21. ATTRIBUTION OF THE JULY 2016 EXTREME PRECIPITATION EVENT OVER CHINA'S WUHAN

Chunlüe Zhou, Kaicun Wang, and Dan Qi

Human-induced warming and El Niño may have substantially increased the probability of the occurrence of such events as the July 2016 extreme precipitation over China's Wuhan.

Introduction. From 30 June to 6 July 2016 Wuhan City, which has approximately ten million residents, received a record-breaking weekly rainfall of 574 mm, reaching a maximum of 1087.2 mm in the downtown areas. This intense rainfall resulted in a disastrous flood that killed 237 people, left 93 people missing, and caused at least $22 billion in damage (U.S. dollars), making it the second most expensive weather-related natural disaster in China's history.

The 2016 Wuhan extreme precipitation was a part of Mei-yu rain (called Baiu in Japan), which has been shown to become particularly heavy in the summer following an El Niño event (Huang et al. 2000; Lin and Lu 2009; Jin et al. 2016). Two ENSO-related processes were proposed to explain this phenomena: 1) the persistent western North Pacific anticyclonic anomaly in the lower troposphere due to the ENSO-related wind–evaporation–SST feedback (Wang et al. 2000; Lau and Weng 2001; Lim and Kim 2007; Chou et al. 2009; Jin et al. 2016; Zhang et al. 2016), and 2) the southward displacement of the Asian jet stream in the upper troposphere due to the increasing meridional temperature gradient and the thermal wind balance that are forced by the ENSO-related warming in the tropical troposphere (Seager et al. 2003; Lin and Lu 2009; Lin 2010). Both processes can transport more moisture to the middle–lower valley of the Yangtze River and induce more precipitation extremes.

The meridional propagation of the Mei-yu front can be quantified by the pattern of R7x (defined as the wettest period over seven consecutive summer days; Fig. 21.1a). The Mei-yu front is typically located over the south coast of China in May, propagates north to the Yangtze River basin by June and to northern China by July, and retreats in August with the end of the East Asian monsoon (Chang et al. 2000).

Using the R7x from the observed and simulated precipitation data, this study tried to answer two questions: 1) How extreme is the 2016 Wuhan extreme precipitation in historical context? 2) What are the relative impacts of the recent El Niño event and human-induced warming on the precipitation extreme?

Data and methods. The latest daily precipitation from 1961 to 2016 at ~2400 meteorological stations (Fig. ES21.1) were used in this study. To better show the spatial variability of precipitation, the hourly precipitation in 2016 at ~50 000 auto weather stations in China were used in Fig. 21.1a. These datasets have undergone a series of quality control tests including outlier identification, internal consistency checks, and spatial and temporal consistency checks (Ren et al. 2010; Shen and Xiong 2016).

The Niño-3.4 index derived from HadISST over the region (5°S–5°N, 170°–120°W; Rayner et al. 2003) was calculated for December–February (DJF). Model data were extracted from the CMIP5 archive (Taylor et al. 2011). We evaluated their performance in capturing the observed variabilities of precipitation and the DJF Niño-3.4 index via a Kolmogrov–Smirnoff test ($p > 0.05$; failure to reject the null hypothesis that the modeled precipitation has the same distribution as the observed). The simulations with standard deviations greater than 1.47°C (1.5σ) in the Niño-3.4 index were excluded, because the overestimated ENSO variability can result in its spurious relationship with the East Asia summer rainfall (Fu et al. 2013).

To separate the influences of the El Niño and La Niña events, we further evaluated and selected the all-forcing (ALL) simulations with a significantly positive relationship ($p < 0.1$) between the detrended precipitation and DJF Niño-3.4 time series. The years with the DJF Niño-3.4 index above (below) 0.98°C

AFFILIATIONS: Zhou and Wang—College of Global Change and Earth System Science, Beijing Normal University,Beijing,China; Qi—National Meteorological Center, China Meteorological Administration, Beijing, China

DOI:10.1175/BAMS-D-17-0090.1

A supplement to this article is available online (10.1175/BAMS-D-17-0090.2)

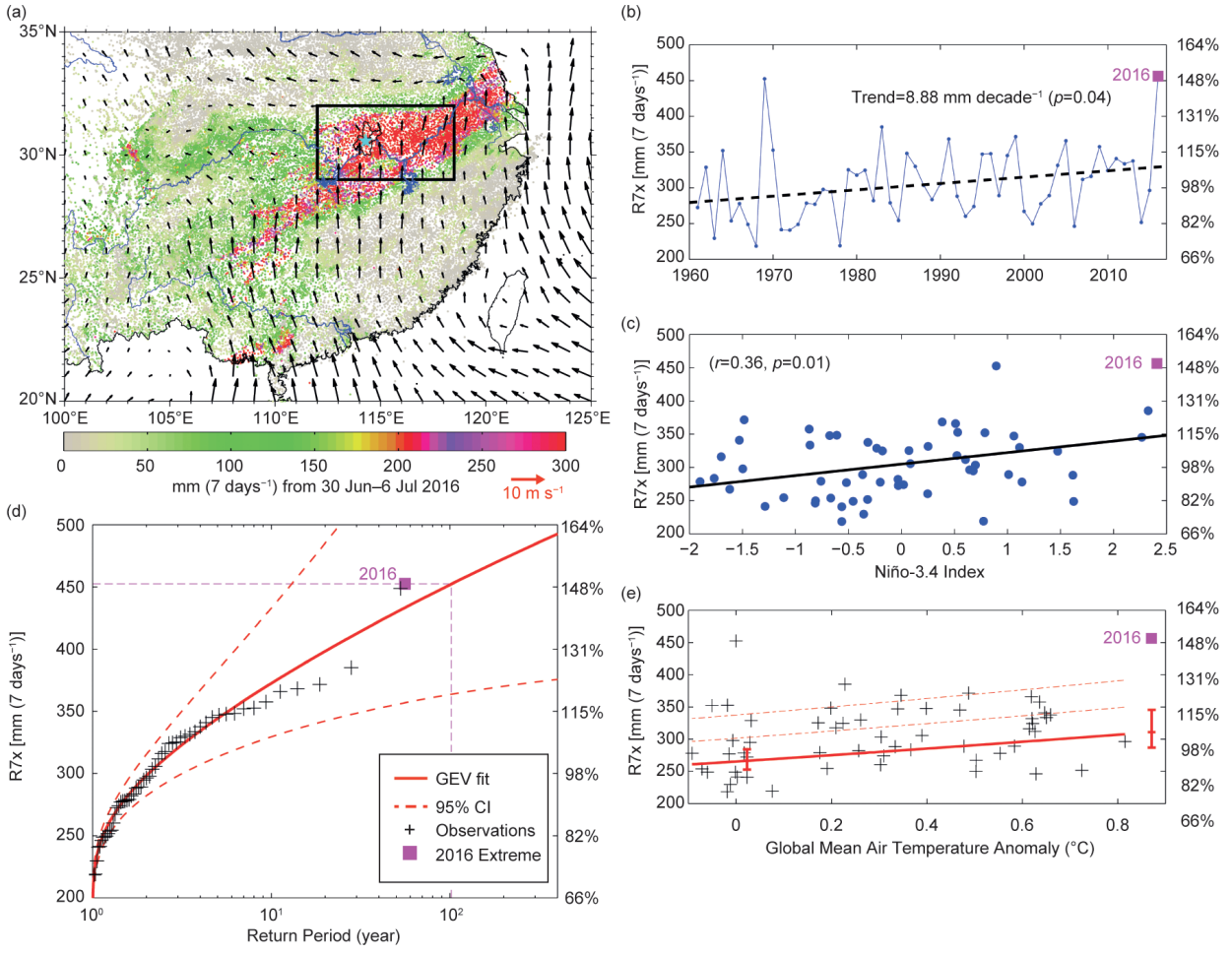

Fig. 21.1. (a) Spatial pattern in precipitation accumulation (R7x, in station dots) and 10-m wind field (in black arrows) during 2016 Wuhan extreme precipitation (30 Jun to 6 Jul 2016). Cyan pentagram shows Wuhan City, China. Blue lines indicate first-class rivers in China. Black rectangle denotes study region (29°–32°N, 112°–118°E). (b) Time series of R7x for black boxed region. 2016 is marked in pink square. (c) R7x for black box region during 1961–2016 is illustrated with DJF Niño-3.4 index. Right axis denotes normalized value (1961–2016 average of R7x). Correlation coefficient is 0.36 ($p < 0.01$), which is almost same as that from detrended series (0.37, $p < 0.01$). (d) GEV fit (in red line) of R7x with 95% confidence intervals (dashed lines). (e) Scaled GEV fit of R7x in which location parameter (thick red line) and scale parameter (difference between red lines) depend exponentially on global mean air temperature anomaly with ratio of two parameters being constant.

(1σ) in the observation and model simulations were regarded to be El Niño (La Niña) years (Black and Karoly 2016; King et al. 2016; Lehner et al. 2016). As a result, 13% (11%) of the years from the twelve models were selected (Table ES21.1).

These CMIP5 models provide 35 simulations with all-forcings (ALL) and natural forcings only (NAT). The ALL runs were extended through 2016 with the Representative Concentration Pathways (RCP) 8.5, because the projected greenhouse gas forcing of RCP8.5 is more consistent with present values than other RCPs (Peters et al. 2013). Values of R7x were estimated with fewer simulations, as three of the models did not provide the necessary daily rainfall data.

We further used model data from a pair of multidecadal ensemble experiments using the latest Met Office HadGEM3-A-based attribution system (N216 L85, 0.83° × 0.56° resolution; Christidis et al. 2013). This attribution system adopts the latest operational dynamical core (Wood and Stainforth 2010) and land surface model (JULES; Best et al. 2011), as well as an updated set of forcings consistent with the CMIP5 generation (Jones et al. 2011). Additionally, this attribution system comprises two sets of 15 stochastic physics experiments spanning the period 1960–2015, one set with all-forcings and the other with natural forcings only. The observed sea surface temperature and sea ice data from HadISST provided a better

estimation of the boundary conditions for the two sets of runs (Christidis et al. 2013).

For consistency with our observational analysis, the model data are area-averaged over the study region (29°–32°N, 112°–118°E; Fig. 21.1a). In addition to R7x, we also did the analysis for monthly (July) precipitation. We applied several statistical techniques to assess the 2016 Wuhan extreme precipitation:

1) A Kolmogorov–Smirnoff test (K–S) was conducted to determine how well the distributions of the simulated precipitation and Niño-3.4 index matched the observed distribution.

2) Both the generalized extreme value (GEV; Schaller et al. 2016) and scaled GEV (van der Wiel et al. 2017) were performed to fit the observed precipitation. In the scaled GEV fit, the location and scale parameters depend exponentially on the global mean air temperature anomaly with the ratio of the two parameters being constant (van der Wiel et al. 2017; more details in the online supplement). The scaled GEV can reflect the influence of global warming on the odds of precipitation extremes. Only the GEV was conducted to fit the modeled precipitation here. Their uncertainties (5%–95%) were estimated with a 1000-member bootstrap.

3) The fraction of attributable risk ($FAR = 1 - P_{NAT}/P_{ALL}$) method (Stone and Allen 2005) was used to ascertain the influence of anthropogenic climate change. Bootstrapping (with replacement) was performed 1000 times to estimate the FAR uncertainty.

4) The scaling factors of the simulated extreme precipitation to best match the observations by two-signal analyses of the optimal fingerprinting (OF) method were estimated to evaluate the impact of anthropogenic climate change (Hegerl et al. 1997; Allen and Stott 2003; Ribes et al. 2013). The observed precipitation was regressed onto the multimodel mean precipitation response to NAT and anthropogenic forcings (ANT = ALL − NAT) simultaneously (Wan et al. 2015). A total of 114 chunks, each 55 years long, were obtained from 12 preindustrial control simulations to estimate internal variability (Table ES21.1). Uncertainty ranges (5%–95%) for the scaling factors were evaluated via Monte Carlo simulations. The signal of human-induced warming is considered detected if the scaling factor is significantly greater than zero (Min et al. 2011).

Results. Figure 21.1a illustrates the rainbelt of R7x related to the northward propagation of the Mei-yu front, originating from the South China Sea. Following the 2015/16 strong El Niño event, the study region received a record-breaking average R7x of 456.28 mm. The R7x exhibits a significantly positive correlation with the DJF Niño-3.4 index ($r = 0.36$, $p = 0.01$; Fig. 21.1c).

The R7x over this region shows a significant increasing trend of 8.88 mm decade^{-1} (Fig. 21.1b). Therefore, we considered the covariance of R7x and global warming and found the location parameter of the scaled GEV for the observed R7x exhibits an upward trend (Fig. 21.1e). A GEV fit of the observed R7x denotes that the 2016 Wuhan extreme precipitation was close to a 1-in-106-year event (Fig. 21.1d). Under the global mean air temperature of 1961, the precipitation extreme like the 2016 Wuhan extreme precipitation (normalized value of 149.69%) is a 1-in-272-year event (Fig. 21.2a). However, it becomes a 1-in-28-year event when the observations are shifted up with global mean air temperature of 2016 (Fig. 21.2a).

To assess the influence of human-induced warming, we compared the changes in the likelihood of the R7x anomaly from the ALL and NAT runs (Fig. 21.2a). Given the El Niño events, 64% [95% confidence intervals (CI): 45%–71%; 26% (95% CI: 20%–39%) for the HadGEM3-A-based system] of the attributable risk of such an event as the 2016 Wuhan extreme precipitation is attributed to human-induced warming (Figs. 21.2a and ES21.3a). Given the La Niña events, such events do not occur in NAT scenarios (as indicated by all the green squares below the observed 2016), whose intense precipitation tail agrees well with that scaled with the global mean air temperature of 1961 (Fig. 21.2a). However, such events do exist in La Niña years in the ALL simulations (Fig. 21.2a).

Compared with the likelihood of the R7x anomaly between El Niño and La Niña events in the ALL simulations, we found a 144% [(95% CI: 119%–182%); 216% (95% CI: 192%–253%) for the HadGEM3-A-based system] increase in the likelihood of such an extreme event in El Niño years (Figs. 21.2a and ES21.3a).

Furthermore, the best estimate of scaling factor of the R7x for anthropogenic forcings is 0.92 (CI: 0.08–1.91; 0.86 with CI 0.18–1.63 in the HadGEM3-A-based system), as derived via two-signal analyses (Figs. 21.2b and ES21.2), suggesting the robustness of detectable human influence on the increasing likelihood for such an event as the 2016 Wuhan extreme precipitation. However, the signal of the natural forcings cannot be detected using the OF method (Fig. 21.2b), likely due to its mixture of the El Niño and La Niña years.

We found that the scaling factors of the R7x for anthropogenic forcings are comparable for the CMIP5 models and the HadGEM3-A-based system via the use of OF method. However, the different attributable risks of such an event as the 2016 Wuhan extreme precipitation to anthropogenic climate change are derived by the FAR method, which may be due to various sensitivities of extreme precipitation to El Niño events between the CMIP5 models and the HadGEM3-A-based system.

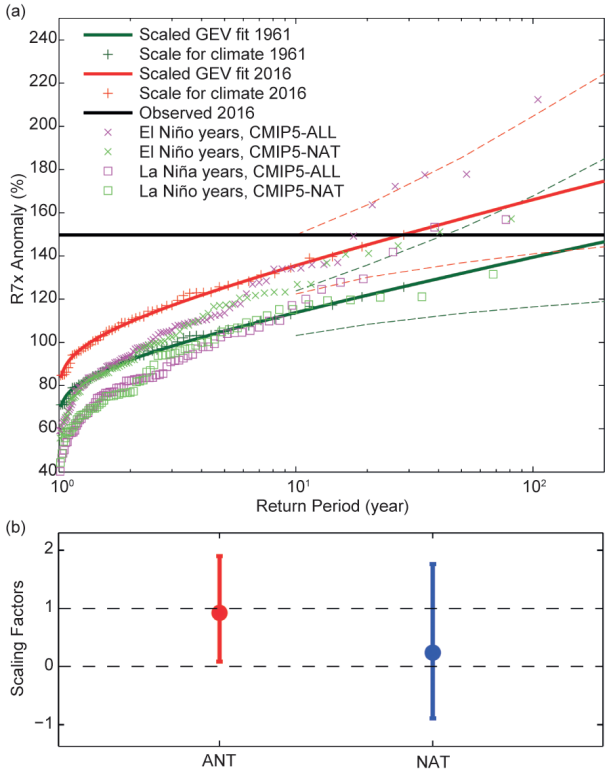

Fig. 21.2. (a) Return period (unit: year) of normalized R7x (1961–2016 average of R7x) from observations and models participating in CMIP5 under different conditions, including ALL and NAT simulations. Pink (green) crosses/squares are in El Niño/La Niña years from ALL (NAT) simulations. Observed R7x is fitted with scaled GEV in which location and scale parameters depend exponentially on global mean air temperature. Red line indicates fit of R7x scaled with global mean air temperature of 2016; dark green line indicates same but for global mean air temperature of 1961. Dashed lines indicate 95% CI. Observations are also plotted twice: one shifted up with trend to 2016 and other shifted down to 1961. GEV is fitted to modeled precipitation. Horizontal black line denotes observed value in 2016. (b) Best estimates of scaling factors of R7x using two-signal analysis of optimal fingerprint method. The 5%–95% uncertainties are estimated by Monte Carlo simulations.

Conclusions and discussion. Our analysis based on R7x indicates that the record-breaking extreme precipitation event of 2016 in China's Wuhan is a 1-in-28-year event in the climate of 2016. It is a 1-in-272-year event in the climate of 1961. CMIP5-based FAR analyses suggest that approximately 60% of the risk of such an event can be attributed to human-induced warming. El Niño has substantially increased the likelihood of such an event as the 2016 Wuhan extreme precipitation by 144%. This study helps to advance our understanding of the role of human-induced warming and El Niño in intense precipitation over East Asia.

If monthly (July) precipitation was used as the index of such an event (normalized value of 260.07% in 2016), 75% [(95% CI: 54%–86%); 21% (95% CI: 17%–29%) for the HadGEM3-A-based system] of the risk can be attributed to human-induced warming using the CMIP5 models (Figs. ES21.3b and ES21.4a), which is consistent with the results based on R7x (Figs. 21.2a and ES21.3a). However, such events do not occur during La Niña years, and anthropogenic forcings make monthly precipitation extremes occur infrequently (Figs. ES21.3b and ES21.4a). Additionally, the signal of human-induced warming in monthly precipitation was significantly detected by the optimal fingerprinting method in the CMIP5 models (Fig. ES21.3c), but not in the HadGEM3-A-based system (Fig. ES21.4b).

We found that the FAR of such events due to human-induced warming in the CMIP5 models is higher than those in the HadGEM3-A-based system, but the increases in the likelihoods of such events in El Niño years compared to those in the La Niña years are smaller in the CMIP5 models than those in the HadGEM3-A-based system. Both the CMIP5 and HadGEM3-A-based system adopt consistent anthropogenic forcings. However, the CMIP5 coupled models have large uncertainties in the modeling of internal variability, and CMIP5 models might be more sensitive to anthropogenic forcings than the HadGEM3-A-based system. The HadGEM3-A-based system tends to better capture the influence of ENSO due to the use of the observed sea ice and sea surface temperature, the latest operational dynamical core (Wood and Stainforth 2010) and its land surface model (Best et al. 2011). Despite all this, the HadGEM3-A-based system does not adopt a fully coupled atmosphere–ocean system, which may introduce some uncertainty when deriving the scaling factor.

ACKNOWLEDGMENTS. This study was funded by the National Basic Research Program of China (2017YFA0603601), the National Natural Science

Foundation of China (41525018) and the Fundamental Research Funds for the Central Universities (312231103). The latest precipitation data were obtained from the China Meteorological Administration (CMA, http://data.cma.cn/). Considerable gratitude is owed to several working teams, including the European Centre for Medium-Range Weather Forecasts (ECMWF) for providing the 10-m wind field, the Global Climate Observing System (GCOS) Working Group on Surface Pressure (WG-SP) for the Niño-3.4 index (www.esrl.noaa.gov/psd/gcos_wgsp/), the Met Office for the HadGEM3-A-based operational event attribution system (http://catalogue.ceda.ac.uk/), the World Climate Research Programme's Working Group on Coupled Modelling (http://cmip-pcmdi.llnl.gov/cmip5/), and the Royal Netherlands Meteorological Institute (https://climexp.knmi.nl/) for the CMIP5 model output.

REFERENCES

Allen, M., and P. Stott, 2003: Estimating signal amplitudes in optimal fingerprinting, Part I: Theory. *Climate Dyn*., **21**, 477–491, doi:10.1007/s00382-003-0313-9.

Best, M., and Coauthors, 2011: The Joint UK Land Environment Simulator (JULES), model description–Part 1: Energy and water fluxes. *Geosci. Model Dev*., **4**, 677–699, doi:10.5194/gmd-4-677-2011.

Black, M. T., and D. J. Karoly, 2016: Southern Australia's warmest October on record: The role of ENSO and climate change [in "Explaining Extreme Events of 2015 from a Climate Perspective"]. *Bull. Amer. Meteor. Soc*., **97**, S118–S121, doi:10.1175/BAMS-D-16-0124.1.

Chang, C.-P., Y. Zhang, and T. Li, 2000: Interannual and interdecadal variations of the East Asian summer monsoon and tropical Pacific SSTs. Part I: Roles of the subtropical ridge. *J. Climate*, **13**, 4310–4325, doi:10.1175/1520-0442(2000)013<4310:IAIVOT>2.0.CO;2.

Chou, C., L.-F. Huang, J.-Y. Tu, L. Tseng, and Y.-C. Hsueh, 2009: El Niño impacts on precipitation in the western North Pacific–East Asian sector. *J. Climate*, **22**, 2039–2057, doi:10.1175/2008JCLI2649.1.

Christidis, N., P. A. Stott, A. A. Scaife, A. Arribas, G. S. Jones, D. Copsey, J. R. Knight, and W. J. Tennant, 2013: A new HadGEM3-A-based system for attribution of weather- and climate-related extreme events. *J. Climate*, **26**, 2756–2783, doi:10.1175/JCLI-D-12-00169.1.

Fu, Y., R. Lu, H. Wang, and X. Yang, 2013: Impact of overestimated ENSO variability in the relationship between ENSO and East Asian summer rainfall. *J. Geophys. Res. Atmos*., **118**, 6200–6211, doi:10.1002/jgrd.50482.

Hegerl, G. C., K. Hasselmann, U. Cubasch, J. F. B. Mitchell, E. Roeckner, R. Voss, and J. Waszkewitz, 1997: Multi-fingerprint detection and attribution analysis of greenhouse gas, greenhouse gas-plus-aerosol and solar forced climate change. *Climate Dyn*., **13**, 613–634, doi:10.1007/s003820050186.

Huang, R., Z. Renhe, and Z. Qingyun, 2000: The 1997/98 ENSO cycle and its impact on summer climate anomalies in East Asia. *Adv. Atmos. Sci*., **17**, 348–362, doi:10.1007/s00376-000-0028-3.

Jin, D., S. N. Hameed, and L. Huo, 2016: Recent changes in ENSO teleconnection over the western Pacific impacts the eastern China precipitation dipole. *J. Climate*, **29**, 7587–7598, doi:10.1175/JCLI-D-16-0235.1.

Jones, C., and Coauthors, 2011: The HadGEM2-ES implementation of CMIP5 centennial simulations. *Geosci. Model Dev*., **4**, 543–570, doi:10.5194/gmd-4-543-2011.

King, A. D., G. J. van Oldenborgh, and D. J. Karoly, 2016: Climate change and El Niño increase likelihood of Indonesian heat and drought [in "Explaining Extreme Events of 2015 from a Climate Perspective"]. *Bull. Amer. Meteor. Soc*., **97** (12), S113–S117, doi:10.1175/BAMS-D-16-0164.1.

Lau, K.-M., and H. Weng, 2001: Coherent modes of global SST and summer rainfall over China: An assessment of the regional impacts of the 1997–98 El Niño. *J. Climate*, **14**, 1294–1308, doi:10.1175/1520-0442(2001)014<1294:CMOGSA>2.0.CO;2.

Lehner, F., A. P. Schurer, G. C. Hegerl, C. Deser, and T. L. Frölicher, 2016: The importance of ENSO phase during volcanic eruptions for detection and attribution. *Geophys. Res. Lett*., **43**, 2851–2858, doi:10.1002/2016GL067935.

Lim, Y.-K., and K.-Y. Kim, 2007: ENSO impact on the space–time evolution of the regional Asian summer monsoons. *J. Climate*, **20**, 2397–2415, doi:10.1175/JCLI4120.1.

Lin, Z.-D., 2010: Relationship between meridional displacement of the monthly East Asian jet stream in the summer and sea surface temperature in the tropical central and eastern Pacific. *Atmos. Oceanic Sci. Lett*., **3**, 40–44, doi:10.1080/16742834.2010.11446840.

——,and R. Lu, 2009: The ENSO's effect on eastern China rainfall in the following early summer. *Adv. Atmos. Sci*., **26**, 333–342, doi:10.1007/s00376-009-0333-4.

Min, S.-K., X. Zhang, F. W. Zwiers, and G. C. Hegerl, 2011: Human contribution to more-intense precipitation extremes. *Nature*, **470**, 378–381, doi:10.1038/nature09763.

Peters, G. P., and Coauthors, 2013: The challenge to keep global warming below 2°C. *Nat. Climate Change*, **3**, 4–6, doi:10.1038/nclimate1783.

Rayner, N., D. E. Parker, E. B. Horton, C. K. Folland, L. V. Alexander, D. P. Rowell, E. C. Kent, and A. Kaplan, 2003: Global analyses of sea surface temperature, sea ice, and night marine air temperature since the late nineteenth century. *J. Geophys. Res.*, **108**, 4407, doi:10.1029/2002JD002670.

Ren, Z. H., and Coauthors, 2010: Quality control procedures for hourly precipitation data from automatic weather stations in China (in Chinese with English abstract). *Meteor. Mon.*, **36**, 123–132.

Ribes, A., S. Planton, and L. Terray, 2013: Application of regularised optimal fingerprinting to attribution. Part I: method, properties and idealised analysis. *Climate Dyn.*, **41**, 2817–2836, doi:10.1007/s00382-013-1735-7.

Schaller, N., and Coauthors, 2016: Human influence on climate in the 2014 southern England winter floods and their impacts. *Nat. Climate Change*, **6**, 627–634, doi:10.1038/nclimate2927.

Seager, R., N. Harnik, Y. Kushnir, W. Robinson, and J. Miller, 2003: Mechanisms of hemispherically symmetric climate variability. *J. Climate*, **16**, 2960–2978, doi:10.1175/1520-0442(2003)016<2960:MOHSCV>2.0.CO;2.

Shen, Y., and A. Xiong, 2016: Validation and comparison of a new gauge-based precipitation analysis over mainland China. *Int. J. Climatol.*, **36**, 252–265, doi:10.1002/joc.4341.

Stone, D. A., and M. R. Allen, 2005: The end-to-end attribution problem: From emissions to impacts. *Climate Change*, **71**, 303–318, doi:10.1007/s10584-005-6778-2.

Taylor, K. E., R. J. Stouffer, and G. A. Meehl, 2011: An overview of CMIP5 and the experiment design. *Bull. Amer. Meteor. Soc.*, **93**, 485–498, doi:10.1175/BAMS-D-00094.1.

van der Wiel, K., and Coauthors, 2017: Rapid attribution of the August 2016 flood-inducing extreme precipitation in south Louisiana to climate change. *Hydrol. Earth Syst. Sci.*, **21**, 897–921, doi:10.5194/hess-21-897-2017.

Wan, H., X. Zhang, F. Zwiers, and S.-K. Min, 2015: Attributing northern high-latitude precipitation change over the period 1966-2005 to human influence. *Climate Dyn.*, **45**, 1713–1726, doi:10.1007/s00382-014-2423-y.

Wang, B., R. Wu, and X. Fu, 2000: Pacific–East Asian teleconnection: How does ENSO affect East Asian climate? *J. Climate*, **13**, 1517–1536, doi:10.1175/1520-0442(2000)013<1517:PEATHD>2.0.CO;2.

Wood, L., and A. Stainforth, 2010: ENDGame Formulation v3.01. Met Office [United Kingdom] paper.

Zhang, W., H. Li, M. F. Stuecker, F.-F. Jin, and A. G. Turner, 2016: A new understanding of El Niño's impact over East Asia: Dominance of the ENSO combination mode. *J. Climate*, **29**, 4347–4359, doi:10.1175/JCLI-D-15-0104.1.